



Surface Melting and Evaporation During Plasma Disruptions in Magnetic Fusion Reactors

A.M. Hassanein, G.L. Kulcinski, and W.G. Wolfer

September 1982

UWFDM-494

Nuclear Engr. and Design **1**, 307 (1984).

FUSION TECHNOLOGY INSTITUTE
UNIVERSITY OF WISCONSIN
MADISON WISCONSIN

DISCLAIMER

This report was prepared as an account of work sponsored by an agency of the United States Government. Neither the United States Government, nor any agency thereof, nor any of their employees, makes any warranty, express or implied, or assumes any legal liability or responsibility for the accuracy, completeness, or usefulness of any information, apparatus, product, or process disclosed, or represents that its use would not infringe privately owned rights. Reference herein to any specific commercial product, process, or service by trade name, trademark, manufacturer, or otherwise, does not necessarily constitute or imply its endorsement, recommendation, or favoring by the United States Government or any agency thereof. The views and opinions of authors expressed herein do not necessarily state or reflect those of the United States Government or any agency thereof.

Surface Melting and Evaporation During Plasma Disruptions in Magnetic Fusion Reactors

A.M. Hassanein, G.L. Kulcinski, and W.G.
Wolfer

Fusion Technology Institute
University of Wisconsin
1500 Engineering Drive
Madison, WI 53706

<http://fti.neep.wisc.edu>

September 1982

UWFDM-494

SURFACE MELTING AND EVAPORATION DURING PLASMA DISRUPTIONS
IN MAGNETIC FUSION REACTORS

A.M. Hassanein^{*}

G.L. Kulcinski

W.G. Wolfer

Fusion Engineering Program
Nuclear Engineering Department
University of Wisconsin-Madison
Madison, Wisconsin 53706

September 1982

UWFDM-494

[†]Submitted to Nuclear Engineering and Design

^{*} Present address: Argonne National Laboratory, Materials Science and Technology Division.

SURFACE MELTING AND EVAPORATION DURING DISRUPTIONS
IN MAGNETIC FUSION REACTORS

A.M. Hassanein

G.L. Kulcinski

W.G. Wolfer

ABSTRACT. Disruptions in tokamaks lead to high energy deposition for short times on in-vessel components. Melting and evaporation may then occur. A comprehensive model to evaluate the extent and duration of melting, the amount of evaporation, and the time for resolidification is presented. This model entails the solution of a heat conduction problem with two moving boundaries, the liquid surface and the melt-solid interface with a surface boundary condition determined by the dynamics of evaporation. Extensive numerical results are presented for in-vessel components made of stainless steel, molybdenum, or graphite. The effects of vapor shielding, pulse shape, and pulse duration are also investigated.

1. Introduction

The existence of plasma disruptions in tokamaks has been known ever since that confinement concept was first introduced by Soviet scientists in 1960 [1]. These disruptions, which still occur with alarming frequency in current devices, deposit large amounts of thermal energy on the metallic vacuum walls or limiters. Large temperature excursions, resulting in melting and in some cases evaporation of the metallic components, have been observed [2,3]. Previous analyses [4-6] of this problem have produced models which can describe the gross features of a thermal excursion but they suffer from oversimplifications (neglect of thermally varying properties, self-shielding by the blow-off vapor, etc.) which can greatly affect the final results. The object of this paper is to develop a model which will incorporate the thermal properties and physical properties of the evaporated layer in a self-consistent manner.

The organization of this paper is as follows. First, we briefly review the range of heat fluxes and deposition times that we might expect from disruptions. Second, we formulate the heat conduction problem with two moving boundaries for the melt-solid and the vapor-melt interface. In conjunction with the moving boundary problem we review the physical basis for evaporation into a vacuum, and we propose a simple model to account for the interaction between the impinging plasma particles and the ejected vapor. In the third part of this paper, a set of sample calculations is presented for the evaporation and melting of first wall components made of stainless steel, molybdenum, and graphite. Finally, the implications of the results are discussed in view of next generation tokamaks such as INTOR [7], FED [8], and a commercial reactor like STARFIRE [9].

2. Plasma Disruption Characteristics

One of the first problems encountered in this type of analysis is the lack of well documented experimental data about disruptions. The exact cause of these plasma instabilities and methods to prevent their occurrence are relatively unknown at this time, so it is generally felt throughout the field that the next generation of large tokamaks will have to be designed to take hundreds to thousands of such disruptions over their lifetime.

The major areas of uncertainty in this field are:

- a) Total amount of plasma and magnetic energy that appears as heat in the first wall or limiter.
- b) Fraction of the total heat flux to the wall which appears as x-rays.
- c) Location of the impact area of the plasma energy.
- d) Peaking factors of the plasma heat flux.
- e) Time over which thermal energy is deposited on the walls.

The most important parameters that need to be determined from the above list are the energy flux (J/cm^2) to the wall and the time duration of that energy flux, τ_d . A schematic of how one arrives at the first quantity is shown in Fig. 1. The thermal energy in the plasma ions and electrons is usually given by:

$$\frac{3}{2} \langle \beta_T \rangle \frac{B^2}{2\mu} V_p \quad (1)$$

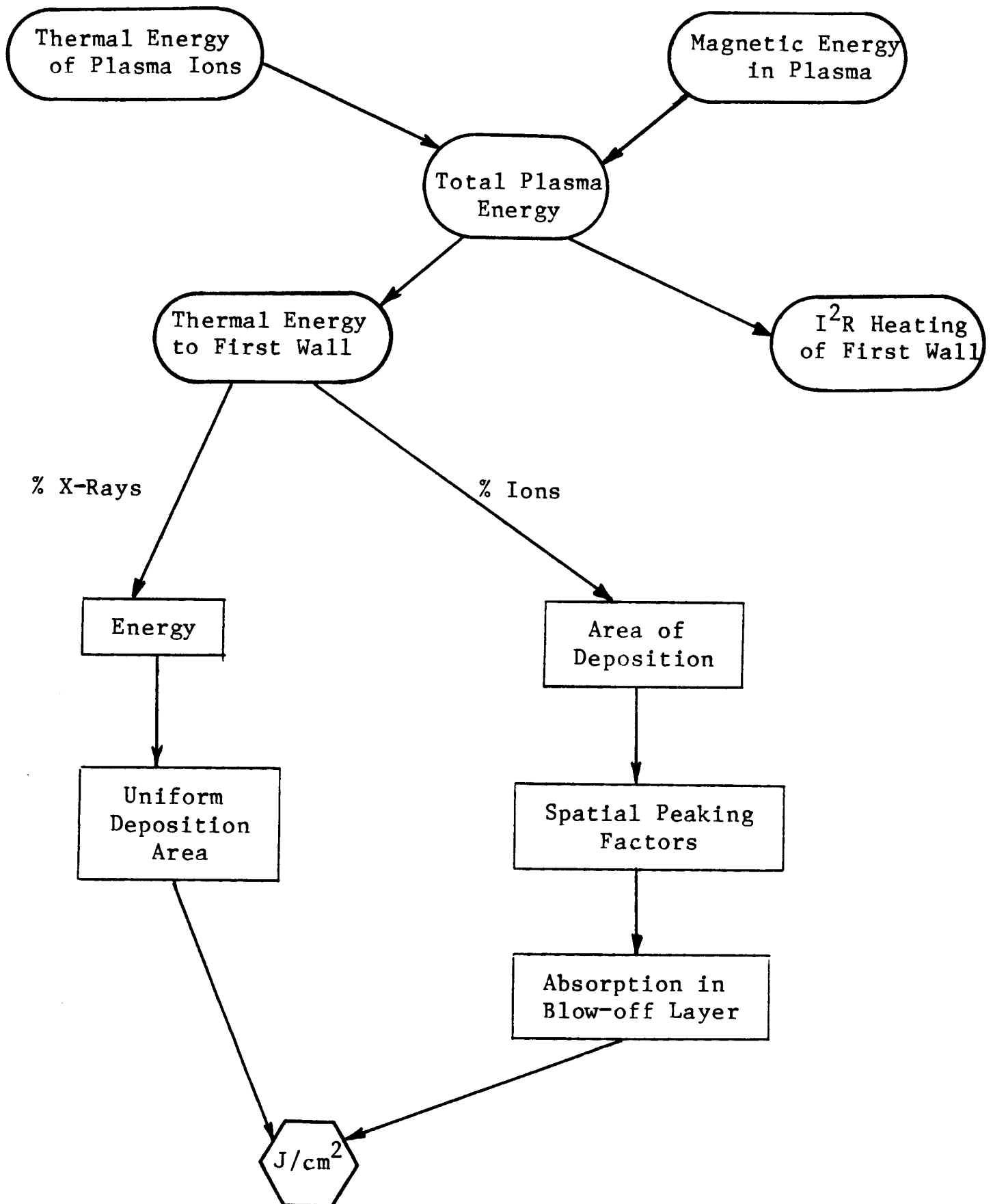
where: $\langle \beta_T \rangle$ = average total beta;

B = magnetic field;

μ = permeability of space;

V_p = plasma volume.

Figure 1 Schematic of factors to be considered for calculating energy deposition densities from plasma disruptions.



The energy stored in the poloidal magnetic field which is the component most easily released on the time scale of a disruption is calculated from

$$\frac{\text{Energy in Magnetic Field}}{\beta_p} \approx \frac{\text{Thermal Energy in Plasma}}{\beta_p} \quad (2)$$

where β_p is the poloidal beta. Typical values for INTOR [7], FED [8], and a commercial STARFIRE [9] are given in Table 1.

The exact amount of stored magnetic energy that appears as I^2R heat in the first wall is also unknown at this time but it is usually assumed to be 50% [10]. The rest of the magnetic energy would then appear as heat in the plasma, via frictional losses as the flux lines move through the plasma.

The next step is to determine how much of the plasma energy goes to the wall as x-rays and how much is transported by ions. Again, the answer to this question depends very much on the device but in general we do know that for extremely "clean" plasmas this fraction can be very low (i.e., a few %) whereas in "dirty" plasmas this could amount to as much as 50% or more. Past assumptions range from 30% in INTOR to 50% in FED, but lower or higher values are also feasible.

The area over which the thermal energy is deposited is usually assumed to be on the inboard side of the tokamak although the top and bottom parts of the vacuum chamber are also possibilities. The inboard area is usually 25-30% of the total chamber surface. Some analyses [8] have assumed that only 1/3 of that area is actually bombarded with plasma ions.

Perhaps the most controversial quantity in the disruption calculation is the uniformity of the energy deposition. It is unreasonable to assume that the plasma will be evenly distributed over the inboard surface of the vacuum

Table 1. Selected Disruption Parameters for Near Term Tokamak Devices

	<u>FED</u>	<u>INTOR</u>	<u>STARFIRE</u>
Average Total Beta - %	5.5	5.6	6.7
B - Tesla	3.6	5.5	5.8
Plasma Volume - m ³	257	241	781
Total Thermal Energy in Plasma - MJ	109	244	1050
Poloidal Beta	1.8	2.6	2.91
Stored Magnetic Field Energy - MJ	61	94	361
Total Stored Energy in Plasma - MJ	170	338	1411
A _w , m ²	366	380	780
Potential Energy Flux During τ_{td} - J/cm ²			
Optimistic ^(a)	65	140	290
Probable ^(b)	220	420	480
Pessimistic ^(c)	2700	5800	12,000
Potential Energy Flux During τ_{cd} - J/cm ²	61	90	170
(f _m = 0.5)			

	<u>f_I</u>	<u>f_x</u>	<u>P</u>	<u>Geometry Factor</u>
Optimistic ^(a)	0.3	0.5	1	2.2
Probable ^(b)	0.2	0.3	2	7.3
Pessimistic ^(c)	0.1	0.1	10	90

f_m = fraction of stored magnetic energy converted into thermal energy of the plasma;

f_x = fraction of plasma thermal energy released as prompt x-rays;

A_w = first wall surface area;

f_I = fraction of A_w that intercepts thermal energy;

P = spatial peaking factor;

$$\text{Geometry factor} = \left[f_x + \frac{(1 - f_x)}{f_i} P \right] .$$

chamber. There is no way to calculate such peaking factors and they have been estimated to be from 2 to 10 times the average heat flux.

The maximum energy flux to the first wall during a disruption is then

$$\left[\left(\frac{3}{2} \langle \beta_T \rangle \frac{B^2}{2\mu} V_p \right) \left(1 + \frac{f_m}{\beta_p} \right) \right] \left[\frac{f_x}{A_w} + \frac{(1 - f_x)}{A_w f_I} P \right] . \quad (3)$$

The final point to consider is the time over which this energy flux strikes the first wall. It is currently thought that there are two time periods of interest; the thermal quench time, τ_{td} , immediately followed by the current quench time, τ_{cd} . The thermal quench time is generally shorter than τ_{cd} . Current values for τ_{td} range from 0.1 ms in Alcator to 0.2 ms in PLT and 0.5 ms in D-III. Estimates of τ_{td} in the next generation of tokamaks range from 5-20 ms, while current decay times are about twice as long.

One might envision the thermal energy striking the wall during the current decay time, τ_{cd} , to be mainly the energy from the magnetic field lines passing through plasma, of f_m/β_p times the plasma thermal energy.

The energy deposited in a time τ_{td} could then be considered to be

$$\left[\frac{3}{2} \langle \beta_p \rangle \frac{B^2}{2\mu} V_p \right] \left[\frac{f_x}{A_w} + \frac{(1 - f_x)}{A_w f_I} P \right] \quad (4)$$

while that deposited in time τ_{cd} immediately following τ_{td} is

$$\left[\frac{3}{2} \langle \beta_T \rangle \frac{B^2}{2\mu} \frac{V_p f_m}{\beta_p} \right] \left[\frac{f_x}{A_w} + \frac{(1 - f_x)}{A_w f_I} P \right] . \quad (5)$$

For typical values of f_I , f_x , and P we can see that the geometry factor ranges from 2 to 90 times the average energy flux if the thermal energy was

spread evenly over the entire first wall surface. For the next generation tokamaks (FED or INTOR) in Table 1, this indicates that probable energy fluxes of $\sim 200 \text{ J/cm}^2$ to $\sim 1000 \text{ J/cm}^2$ are feasible during disruptions. We shall use this range for our calculations in Section 4.

3. Thermal Response of First Wall Components


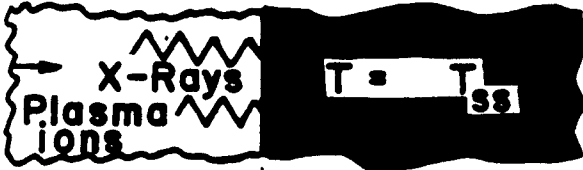
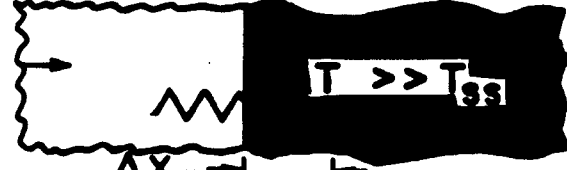

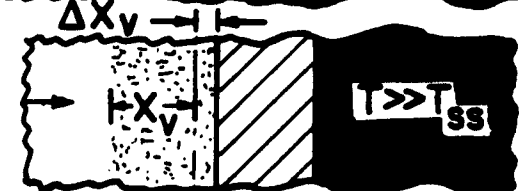
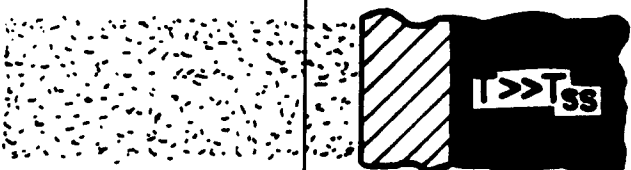
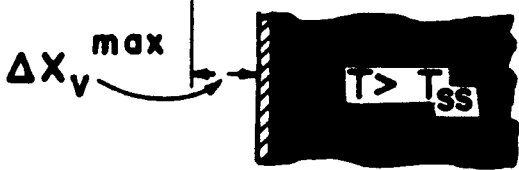

The thermal response of a first wall component exposed to the plasma dump can be divided into a sequence of eight events or phases, illustrated schematically in Fig. 2.

The initial phase prior to the plasma disruption is characterized by a nominal steady state heat flux F_{SS} which determines together with the coolant temperature the steady state temperature distribution T_{SS} through the first wall component. At time $t = 0$, the plasma disruption starts and the heat flux suddenly increases to $F_0 = F_i + F_x$, where the two contributions are due to the plasma particle flux and the x-ray flux, respectively. Strictly speaking, the heat fluxes F_i and F_x should be treated as volumetric energy deposition rates. However, both the ion range and the absorption length of the soft x-rays are very small, so that thermal response is the same for the volumetric and the heat flux deposition.

In the third phase, the temperature rises rapidly in the surface region until the melting point T_m is reached on the surface. During the fourth phase, the melt-solid interface moves deeper into the solid wall while the temperature continues to rise on the melt surface. Evaporation intensifies from the melt surface during the fifth phase until the net heat flux drops because of: (1) vapor shielding, (2) the end of the disruption, or (3) a surface temperature is reached where the energy dissipated by evaporation, conduction, and melting equals the incident energy flux.

Figure 2 Schematic representation of disruption-vaporization process.

SCHEMATIC OF DISRUPTION / VAPORIZATION PROCESS

STEP		TIME	SURFACE Heat Flux
①		$t < 0$	F_{ss}
②		$t = 0$	$F_0 = F_x + F_i$
③		$t_m > t > 0$	F_0
④		$t > t_m$	F_0
⑤		$t > t_v$	$F_0 - F_d(t)$
⑥		$t = t_{Ed}$	~ 0
⑦		$t > t_{Ed}$	0
⑧		$t >> t_{Ed}$	0

During the sixth phase, energy deposition into the first wall has ceased, and the hot melt layer cools by evaporation, radiation, and conduction. Eventually, the temperature on the melt surfaces becomes too low for further evaporation to occur at a significant rate, and the dominant process during this seventh phase is a resolidification of the remaining melt layer. Finally, in the last and eighth phase, the solidified first wall cools further by heat conduction to the coolant or to other structural members.

In the above scenario it was assumed that the melt layer will not be removed, and that it will solidify at the place it was formed. Investigations on the melt layer stability are presently being carried out, and results will be reported elsewhere [11].

3.1 Heat Conduction with Moving Boundaries

The above discussion of the events following a plasma disruption shows that the thermal response of the first wall may be accompanied by two phase changes. Therefore, the heat conduction calculation calls for the solution of a complex moving boundary problem. Although extensive literature exists on such problems, the present problem has apparently not been solved before.*

Whereas most moving boundary or Stefan problems (such as those discussed by Oziski [12], Muehlbauer and Sunderland [13] and in recent conferences [14,15]) deal with melting, solidification, or boiling, where the interface is mathematically characterized by a fixed value of the temperature, the present problem of intense evaporation involves a highly nonlinear boundary condition

* While this work was in progress, the authors have become aware of a similar effort by B. Merrill.

for the surface temperature whose determination is now an integral part of the solution for the entire problem.

Because of this added complication, previous treatments of intense evaporation were based on various simplifying assumptions regarding the condition at the moving boundary. Ready [16] assumed that evaporation begins and proceeds at a constant boiling temperature when the laser pulse duration is large compared to the preheat time for reaching the boiling point. On the other hand, Ready [17] assumed for irradiations with Q-switched lasers that the vapor will be superheated to the critical point, and that the evaporation rate is determined by the thickness of material heated beyond the critical point.

Andrews and Atthey [18] developed a convenient analytical solution to the evaporation problem when it can be assumed that vaporization occurs at a constant boiling point. This solution has been used earlier by Loebel and Wolfer [6] to estimate the erosion by vaporization of various first wall materials. However, melting was neglected in this approach. Behrisch [4] has evaluated the evaporation due to heat pulses when the energy expended for both melting and evaporation is negligible compared to the total energy deposited.

All the above treatments avoid the central problem, namely that the rate of evaporation into a vacuum and the associated surface temperature are entirely determined by the kinetic processes involved in the vaporization, and by the energy partitioning between heat conductions, melting, evaporation, recondensation, and radiation.

Few attempts have been made to solve, in its entirety, this problem of evaporation into a vacuum. Osadin and Shapovalov [19] derived an integral equation for the surface temperature by neglecting melting and the receding motion of the evaporating surface. Golodenko and Kuz'michev [20] included the

boundary motion in an approximate manner, but melting was again neglected, and constant thermophysical properties were assumed. Furthermore, no recondensation was included in any of the treatments.

3.2 Formulation of the Heat Conduction Problem

3.2.1 Without Melting

In view of the shallow penetration depth of heat into the first wall component, we can assume that heat conduction is one-dimensional. Under a heat flux $F(t)$, the temperature distribution $T_s(x,t)$ in the solid phase must then satisfy the heat conduction equation:

$$\rho_s C_s \frac{\partial T_s}{\partial t} - \nabla \cdot k_s \nabla T_s = 0 \quad (6)$$

where the density ρ_s , the specific heat C_s , and the thermal conductivity k_s are in general functions of the temperature. If the location of the surface is at $x = s(t)$, then Eq. (6) has to be solved subject to the boundary condition

$$F(t) = -k_s(T_v) \frac{\partial T_s(s)}{\partial x} + \rho_s(T_v) L_v v(T_v) + \epsilon \sigma (T_v^4 - T_0^4) \quad (7)$$

where $F(t)$ is the heat flux, $T_v = T_s(s,t)$ is the surface temperature, L_v is the heat of vaporization, $v(T_v)$ the velocity of the receding surface, σ is the Stefan-Boltzmann constant, ϵ is the emissivity of the first wall material, and T_0 is the temperature of the first wall surface not exposed to the plasma dump but in direct line of sight of the exposed surface. The last term in Eq. (7) represents the heat radiated to the cold portion of the first wall, the second

term is the power consumed in vaporization, and the first term is the heat conducted into the wall.

3.2.2 With Melting

Once melting commences, the condensed phases of the first wall define two regions: $s(t) < x < m(t)$, and the solid phase in the region $x > m(t)$. Here, $m(t)$ is the instantaneous position of the melt-solid interface.

Equation (6) applies again to the solid region, and a similar equation holds for the melt region. However, the thermophysical properties are different, and they are denoted by a subscript ℓ .

The boundary condition at the melt-solid interface is now

$$k_s \frac{\partial T_s}{\partial x} - k_\ell \frac{\partial T_\ell}{\partial x} = \rho_s L_f w(t) \quad \text{at } x = m(t) \quad (8)$$

where

$$w(t) = \frac{dm}{dt} \quad (9)$$

is the velocity of the moving interface and L_f is the latent heat of fusion.

On the surface of the melt layer at $x = s(t)$, the boundary condition is

$$F(t) = -k_\ell \left. \frac{\partial T_\ell}{\partial x} \right|_s + \rho_\ell (T_v) L_v v(T_v) + \epsilon \sigma (T_v^4 - T_o^4) \quad (10)$$

i.e. identical to Eq. (7) with the solid thermophysical properties replaced by those of the melt layer.

3.2.3 Method of Solution

It will be shown below that the evaporation velocity v is a highly non-linear function of the surface temperature. Furthermore, if temperature dependent thermal properties are used, then the above equation for heat con-

duction must be solved by numerical methods. In the present paper, a finite difference scheme was employed with an interval spacing that increases with increasing depth. Since one of the most critical parameters to be obtained is the thickness of the evaporated layer, an extremely fine interval spacing is required close to the surface. Nevertheless, in order to obtain an accurate result for evaporation thicknesses on the order of microns, a stationary frame for the intervals is not very suitable. Accordingly, it is advantageous to introduce a coordinate frame which moves with the receding surface. Hence, in a frame

$$z(t) = x - s(t) \quad (11)$$

the surface remains always at $z = 0$, but the heat conduction equation (6) transforms into

$$\rho C \frac{\partial T}{\partial t} - \rho C v(T_v) \frac{\partial T}{\partial z} - \nabla \cdot k \nabla T = 0 \quad (12)$$

which differs from the original equation by the convection term $\rho C v(T_v) \partial T / \partial z$. All boundary conditions retain their original form given above, and only $\partial T / \partial x$ is replaced by $\partial T / \partial z$. Equation (12) is solved numerically based on the implicit method of Crank and Nicholson [21]. If there are N interval mesh points, this method involves the simultaneous solution of N algebraic equations. This nonlinear system of equations was solved by iteration, using in each iteration an implicit alternating direction method as suggested by Peaceman and Rachford [22] to solve a system of N linear equations. Double precision was used throughout the entire calculation.

Since the melt front moves with a different velocity than the receding surface, it crosses the nodal point at discrete times. The interval adjacent to the melt front was assumed to become molten (or solidified) whenever the thermal energy gained (or lost) becomes equal to the required heat of fusion for this interval. During the time period required to transform the material in the entire interval, the temperature is assumed to be equal to the melting point.

4. Evaporation Model

According to the Hertz-Knudsen-Langmuir theory of evaporation and condensation [23] the net flux of atoms leaving the surface of the condensed phase is given by

$$J = (2\pi mkT)^{-1/2} (\sigma_e P_s - \sigma_c P_c) \quad (13)$$

where J is the net evaporation flux, m the mass per atom, k the Boltzmann constant, σ_e and σ_c the coefficients for evaporation and condensation, P_c the ambient partial vapor pressure, and P_s is the saturation vapor pressure. The coefficients σ_e and σ_c are used to compensate for nonideal evaporation or condensation. They are usually taken to be the same. The saturation vapor pressure, P_s , is given by

$$P_s = P_0 \exp(-\Delta H/kT) \quad (14)$$

where P_0 is a constant and ΔH is the activation energy for evaporation. Equation (13) consists of two opposite fluxes, $J = J_e - J_c$, an evaporation and a condensation flux.

Although Eq. (13) is valid only for thermal equilibrium, it can be modified for non-equilibrium evaporation or condensation. If the surface temperature T_v of the condensed phase is different from the temperature T_c of the ambient vapor, the evaporation and condensation flux may be written as

$$J_e^{\text{eq}} = (2\pi mkT_v)^{-1/2} \sigma_e P_s(T_v) \quad (15)$$

and

$$J_c = (2\pi mkT_c)^{-1/2} \sigma_c P_c. \quad (16)$$

The evaporation flux J_e^{eq} represents a maximum for evaporation into a vacuum provided the vapor expands at a sufficient rate so the vapor density in front of the surface always remains low.

The net evaporation flux may be computed according to

$$J = J_e^{\text{eq}}(T_v) - J_c(T_c) \quad (17)$$

if the two fluxes do not interact. This will only be the case for slow evaporation, i.e. when both J_e^{eq} and J_c are small or when they are almost of equal magnitude.

Unfortunately, for conditions encountered for example in a plasma disruption, Eq. (17) cannot be considered valid. Since the evaporation flux is expected to be high, the vapor density in front of the surface is finite even if the vapor gas expands into a vacuum. As a result, J_v^{eq} is not the maximum evaporation flux into a vacuum for intense evaporation.

One may be tempted to assume that the maximum evaporation flux is determined by the velocity of an adiabatically expanding gas. Therefore, we

consider for the moment a gas of initial density n and initial temperature T_v . It expands into one direction with a maximum velocity of [24]

$$U_{\max} = 4 c_0 \quad (18)$$

where

$$c_0 = \sqrt{\gamma k T_v / m} \quad (19)$$

is the speed of sound in a gas of temperature T_v and density n , and γ is the ratio of the specific heats for constant pressure and constant volume. For a monatomic gas, $\gamma = 5/3$.

The maximum flux of evaporated atoms according to this model would be given by

$$J_e^{\max} = 4 c_0 n_s = 4 \left(\frac{3kT_v}{2m} \right)^{1/2} \frac{P_s}{kT_v} = 4\sqrt{3\pi} J_e^{\text{eq}} . \quad (20)$$

Since this is larger than J_e^{eq} , we conclude that hydrodynamic considerations alone cannot be invoked to limit the rate for intense evaporation below the maximum equilibrium rate.

It is therefore necessary to derive the rate of recondensation of the expanding vapor from gas-kinetic considerations. In an early analysis by Schrage [25], the vapor is treated as a gas with a Maxwellian velocity distribution superimposed on an average velocity \bar{u} . This average velocity must be equal to the average forward velocity of a stationary Maxwellian gas. Hence

$$\bar{u} = (kT_v / 2\pi m)^{1/2} . \quad (21)$$

the fraction of recondensing atoms is now given by [25]

$$\Gamma = \exp(-a^2) - a\sqrt{\pi} \operatorname{erfc}(a) \quad (22)$$

where

$$a = \bar{u}/v_0$$

and

$$v_0 = \sqrt{2kT_v/m}$$

is the most probable velocity of the Maxwellian gas. Then, a can be written as

$$a = \frac{1}{2\sqrt{\pi}} = 0.282 .$$

The net evaporation flux is now equal to

$$J = J_e^{\text{eq}} \left(1 - \frac{\sigma_c}{\sigma_e} \Gamma \right) . \quad (23)$$

Assuming that the coefficients of condensation and evaporation are equal, i.e. $\sigma_c = \sigma_e$, one obtains $a = 0.282$, and a maximum net evaporation flux of

$$J = 0.422 J_e^{\text{eq}} . \quad (24)$$

More accurate transport calculations for intense evaporation have been performed recently by Anisimov and Rakhmatulina [26]. In their work the following problem was considered. The surface of a material which occupies the half-space is suddenly raised and held at a constant surface temperature T_v

for times $t > 0$. The material begins to vaporize and the vapor expands freely into the vacuum. Initially, the evaporation flux leaving the surface is equal to J_e^{eq} , but it decreases thereafter due to recondensation. This process of recondensation arises from two facts. First, the density of vapor expanding into a vacuum retains a finite value for $t > 0$ in front of the surface. Second, atoms evaporated subsequently from the surface may collide with the already present vapor phase and can be backscattered towards the surface where they may be reabsorbed. The fraction of recondensing atoms will increase as the vapor density and the spatial extension of the vapor phase increases with time. However, an asymptotic value of 0.2 is reached for this fraction after about 20 collision times. The collision time τ_c for the vapor atoms is given by

$$\frac{1}{\tau_c} = 16\sqrt{\pi} n a_0^2 (kT_v/m)^{1/2} \quad (25)$$

where πa_0^2 is the elastic scattering cross section for the vapor atoms and n is the vapor density in front of the surface. The latter can be related to the maximum vacuum evaporation rate according to

$$J_e^{\text{eq}} = \frac{1}{4} \bar{v} n = n (kT_v/2\pi m)^{1/2} \quad (26)$$

where we used the relation

$$\bar{v} = (8kT_v/\pi m)^{1/2}$$

for the average velocity of the vapor atoms.

For the elastic scattering cross section we may use the approximation that

$$\frac{4\pi}{3} a_0^3 = \Omega$$

where Ω is the atomic volume. Then, the collision time τ_c is given by

$$\frac{1}{\tau_c} = 16\sqrt{2} \pi^{1/3} \left(\frac{3}{4} \Omega\right)^{2/3} J_e^{\text{eq}} . \quad (27)$$

The numerical results of Anisimov and Rakhmatulina for the time-dependent net evaporation rate may be approximated by

$$J(t) = J_e^{\text{eq}} [0.8 + 0.2 \exp(-t/\tau_R)] \quad (28)$$

where τ_R is defined as a relaxation time for full recondensation. The relaxation time τ_R to reach, say, 98% of the full amount of recondensation after 20 collision times τ_c , is then given by

$$\tau_R = 20 \tau_c / \ln 10 \cong 10 \tau_c$$

or

$$\frac{1}{\tau_R} = 1.6\sqrt{2} \pi^{1/3} \left(\frac{3}{4} \Omega\right)^{2/3} J_e^{\text{eq}} . \quad (29)$$

In the above equations, $J_e^{\text{eq}}(T_v)$ is a constant for $t > 0$, since it was assumed that T_v remains constant.

For our present application, however, the surface temperature $T_v(t)$ varies with time. Nevertheless, as the numerical results in the following

section show, the surface temperature rapidly approaches a saturation value once intense evaporation begins. Accordingly, the time variable in Eq. (28) should be replaced by $(t - t_v)$ where the preheat time t_v may be estimated as follows.

In order for recondensation to become significant, the thickness of the vapor zone in front of the surface should be on the order of the mean free collision path

$$\ell = [\sqrt{2} n \pi a_0^2]^{-1} .$$

The thickness Δx of material evaporated to produce a vapor zone of thickness ℓ is then

$$\Delta x(t_v)/\Omega = n\ell$$

$$\text{or} \quad \Delta x(t_v) = \frac{1}{\sqrt{2} \pi} \left(\frac{4}{3}\right)^{2/3} \left(\frac{\Omega}{\pi}\right)^{1/3} = 0.585 \Omega^{1/3} \quad (30)$$

and in terms of a_0 , $\Delta x(t_v)$ can be written as

$$\Delta x(t_v) = \frac{4}{3\sqrt{2}} a_0 . \quad (31)$$

This corresponds roughly to a monolayer of atoms evaporated from the surface. The relationship in Eq. (31) determines the preheat time t_v .

The evaporation flux of atoms is then equal to J_e^{eq} , for $t < t_v$ and

$$J(t) = J_e^{\text{eq}}(T_v(t)) [0.8 + 0.2 \exp(-(t - t_v)/10\tau_c)] \quad (32)$$

for $t > t_v$. It should be noted that the collision time τ_c is a very strong function of the surface temperature through its dependence on J_e^{eq} . Therefore, if we consider τ_c as a function of time, it will be a very large number before intense evaporation commences, i.e. for $t < t_v$. As a result, the second term in Eq. (28) will then be equal to 0.2, so that automatically $J(t) \cong J_e^{eq}$, for $t < t_v$. Therefore, by considering the collision time τ_c as a continuous function the changing surface temperature $T_v(t)$, the Eqs. (28) and (32) are practically identical. In other words, it is not necessary to compute the preheat time t_v in order to obtain the time-dependent evaporation flux $J(t)$ correctly according to Eq. (28).

Finally, we note that the velocity of the receding surface is given by

$$v(t) = \Omega J(t) . \quad (33)$$

5. Vapor Shielding

The heat flux $F(t)$ on the first wall during a disruption in a magnetic fusion reactor consists to a large part of the plasma ions. It is generally believed that a sheath potential on the order of 10 keV exists at the onset of the plasma disruption. The plasma ions will therefore strike the first wall with a kinetic energy of about 1-10 keV [27]. For the present study the upper energy of 10 keV was chosen. The average range of the plasma ions in a stainless steel wall is about 7.5×10^{-8} m. Because of this short range, it is indeed appropriate to treat the energy deposition as a surface heat flux rather than a volumetric heat deposition.

On the other hand, if a vapor layer of sufficient thickness has been produced, the plasma ions will be stopped in this vapor layer rather than in the

condensed material of the first wall. The vapor layer, in the process of stopping the plasma ions, will be partially ionized, excited, and heated. Subsequently, the energy stored in this vapor layer will be emitted in the form of x-rays, optical radiation, and thermal diffusion of the hot vapor atoms. As a result, the energy flux of the plasma particles is converted from a unidirectional one into a more isotropic one. If we assume in fact that the converted energy flux has become isotropic, only one half of the original, unidirectional energy flux will now strike the part of the first wall exposed to the plasma disruption.

Accordingly, we have modeled the effect of vapor shielding in the following manner. If F_0 is the magnitude of the initial energy flux, and R the range of plasma ions in the condensed phase of the first wall, a vapor layer produced by the evaporation of a thickness $\Delta x(t) < R$ will reduce the surface heat flux to the first wall to the value of

$$F(t) = F_0[1 - \Delta x(t)/R] + \frac{1}{2} F_0 \Delta x(t)/R = F_0[1 - \Delta x(t)/2R] . \quad (34)$$

When the evaporation thickness $\Delta x(t) > R$, then

$$F(t) = \frac{1}{2} F_0 . \quad (35)$$

Figure 3 shows schematically the effect of vapor shielding on the surface heat flux according to the present model and for a constant plasma particle flux during the disruption time.

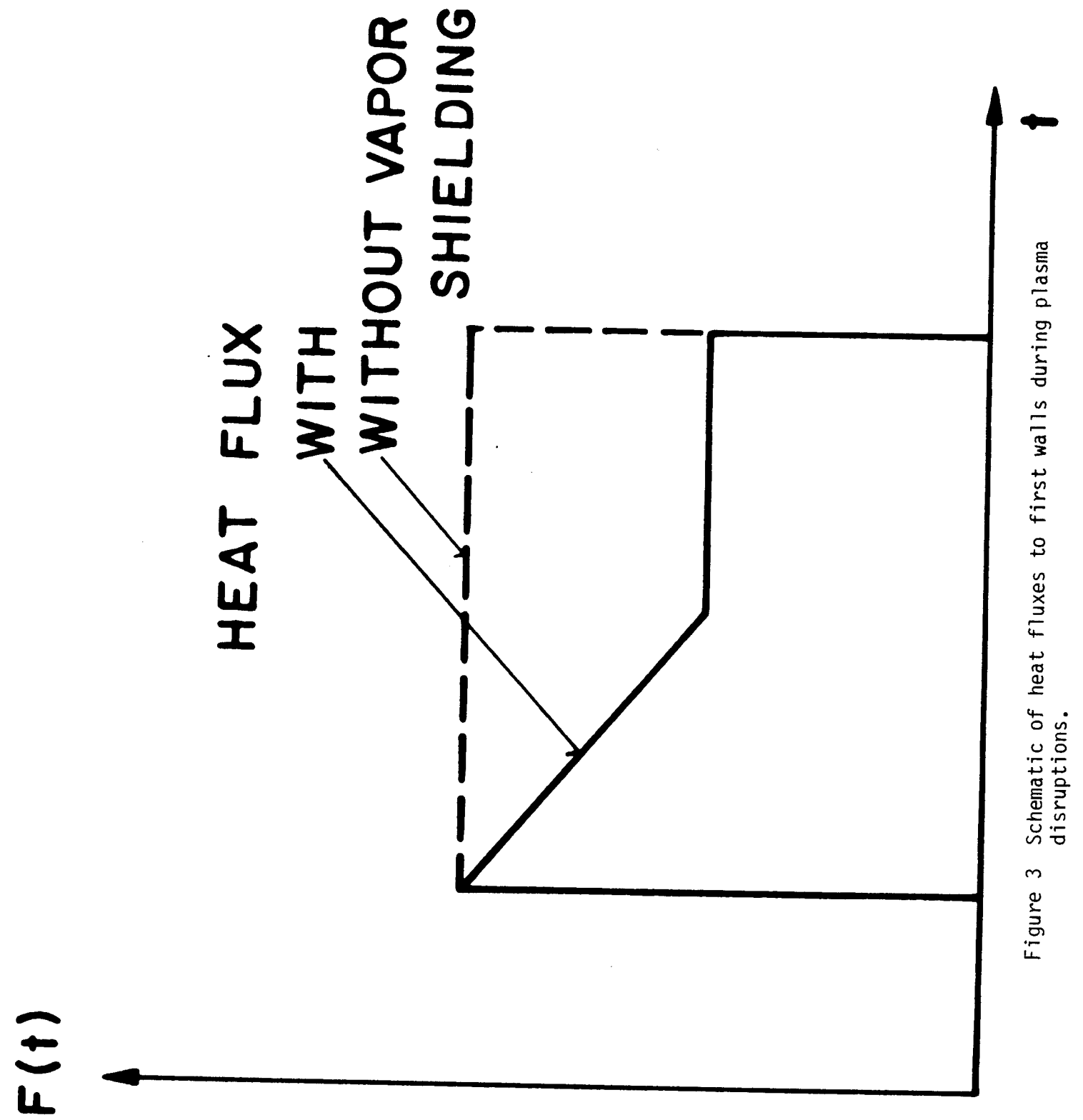


Figure 3 Schematic of heat fluxes to first walls during plasma disruptions.

6. Parametric Analysis

The A*THERMAL [28] computer code is used to evaluate the response of the first wall due to plasma disruptions. The code is developed to provide analysis of the energy deposition, temperature response, melted and vaporized thickness of first walls and other subsequent effects produced in materials such as displacement production and sputtering erosion. The solution to the problem of ion and photon transport, radiation energy deposition and heat conduction with two moving boundaries is sufficiently efficient to allow parametric and simultaneous analysis of a wide range of applications.

The estimated deposition times for plasma disruptions vary widely as discussed before, but it is generally agreed that they are on the order of or less than 100 ms. Longer deposition times result in lower surface temperatures than shorter times. In order to explore this parametric dependence, the present calculations were carried out for deposition times equal to 5, 10, and 20 ms, and for energy densities as large as 1300 J/cm^2 . Furthermore, it was assumed that the energy is deposited at a constant rate over the assumed disruption time. The effect of different pulse shapes was studied in some cases by examining the response to a triangular pulse and comparing the result to that of a square pulse shape.

Three materials are considered in this analysis, stainless steel (SS), carbon, and molybdenum. Steel and carbon are two of the main candidate materials for structural or limiter components in fusion reactors. Because the high temperature, refractory metals offer a range of properties that makes them unique among the candidate materials for limiters in fusion reactors, molybdenum was chosen in this analysis. Most of the results shown will be for SS, however.

7. Results and Discussion

Due to the large number of parameters involved in this study (different materials used, different amounts of energies deposited, different pulse shapes), the results are presented in the following order. First the surface temperature as a function of time is shown for stainless steel and for the three disruption times considered in this analysis, i.e. 5, 10, and 20 ms. Three values of energy density have been used in the calculations: 325, 650, and 1300 J/cm². The melting zone thickness as a function of the input energy density is shown next for stainless steel. The velocity of the receding surface is shown as a function of time. Finally, the effect of the vapor shielding on the surface temperature, melting zone thickness, and the amount of material evaporated is also illustrated. Disruption times as low as 100 μ s and as large as 100 ms have been considered.

Any combination of different values other than the ones considered here could be easily obtained from the computer code A*THERMAL, and the following example represent typical results.

7.1 Surface Temperature

The surface temperature of stainless steel (SS) as a function of time for the three energy densities, i.e. 325, 650, and 1300 J/cm², is shown in Figs. 4, 5, 6, respectively. All the plots shown in this study are for the case of no vapor shielding unless explicitly stated. The thermophysical properties used in this work are those given in Refs. [29-32], and the initial temperature is assumed to be $T_0 = 573^\circ\text{K}$. Each curve is shown for the three disruption times considered, i.e. 5, 10, and 20 ms. It is seen in Fig. 4 that the surface temperature rapidly exceeds the melting temperature of SS ($T_m = 1700^\circ\text{K}$) for any of the disruption times considered. The shorter the

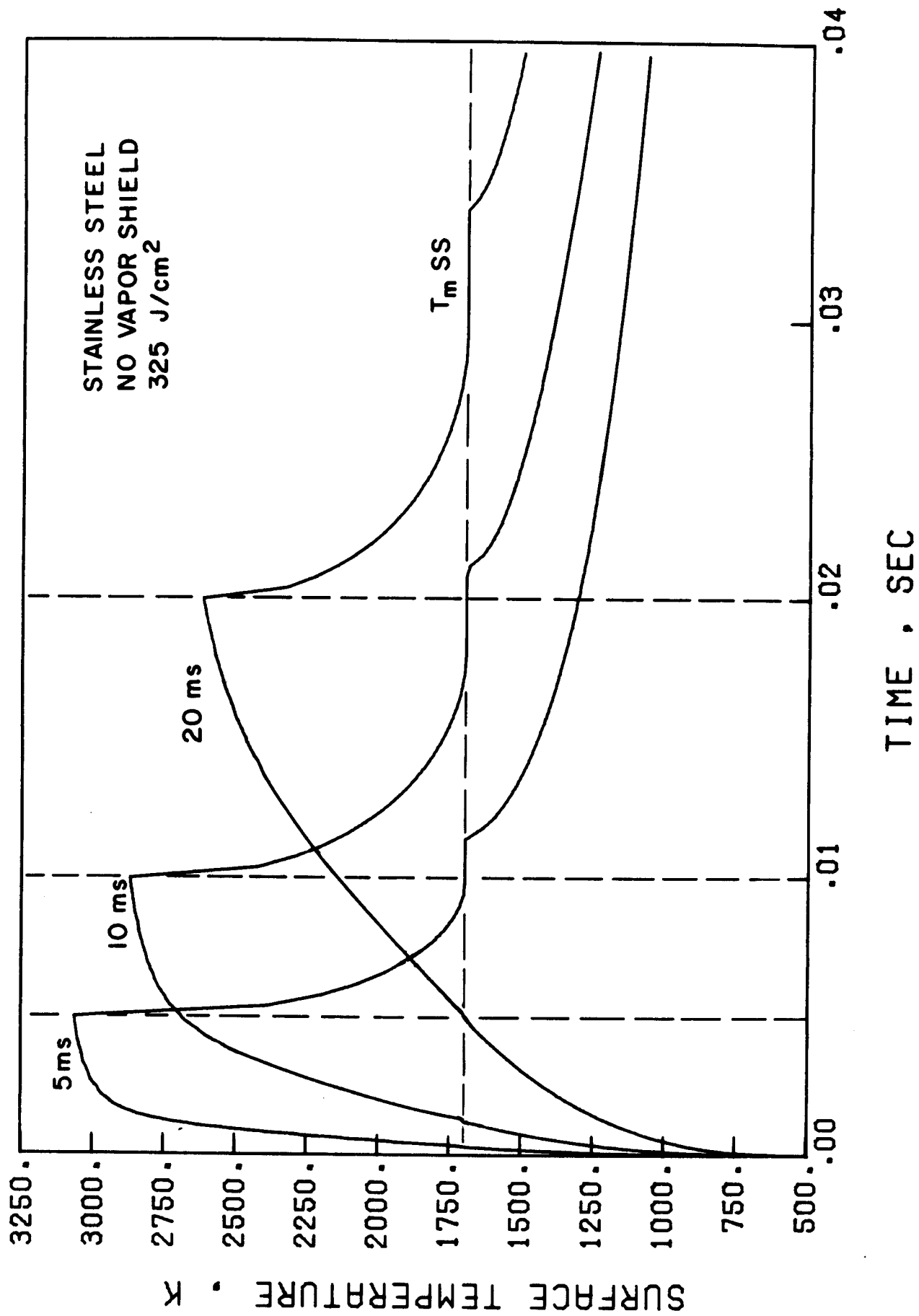


Figure 4 Surface temperature rise of stainless steel for energy density of 325 J/cm² and different disruption times (no vapor shielding).

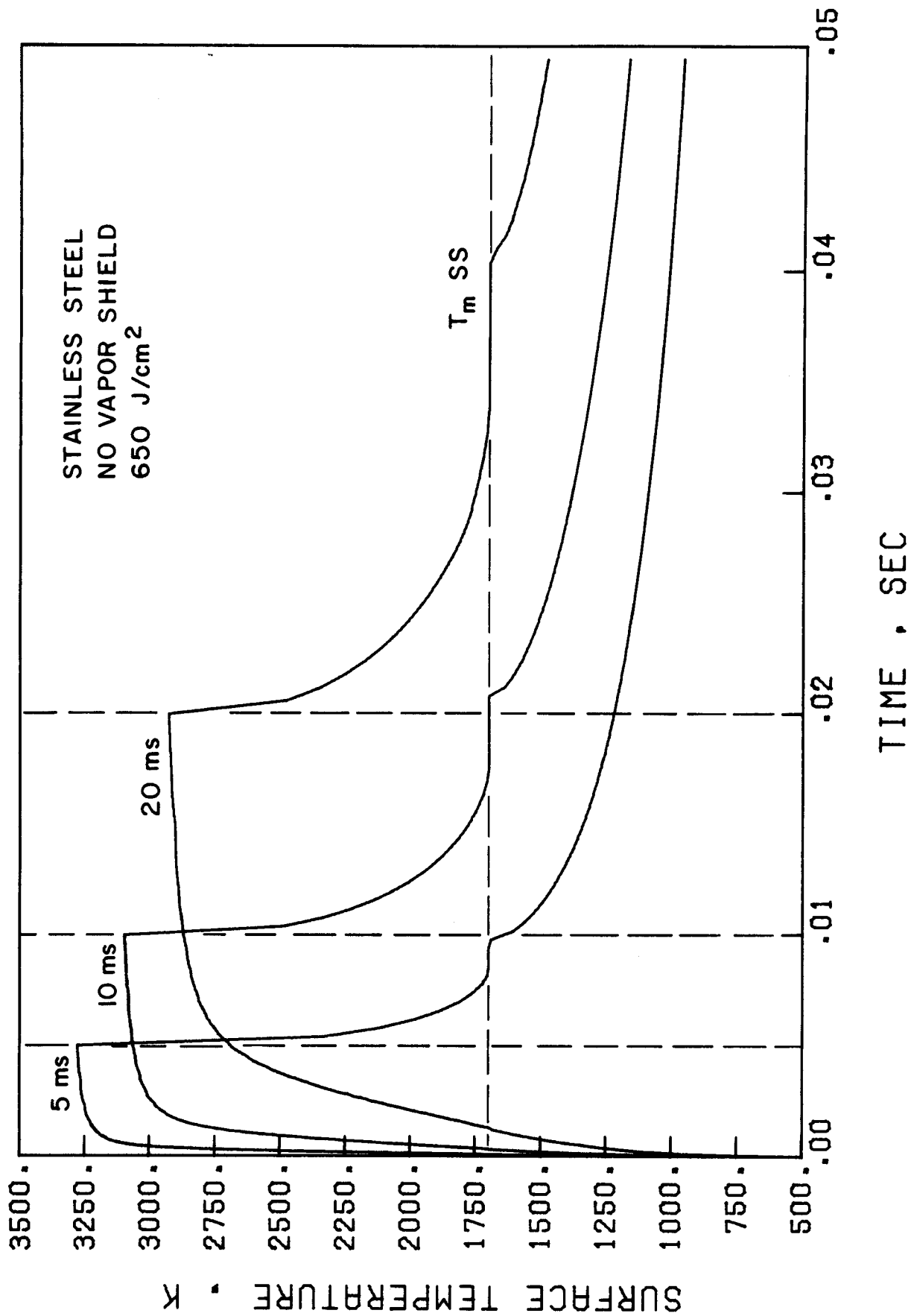


Figure 5 Surface temperature rise of stainless steel for energy density of 650 J/cm² and different disruption times (no vapor shielding).

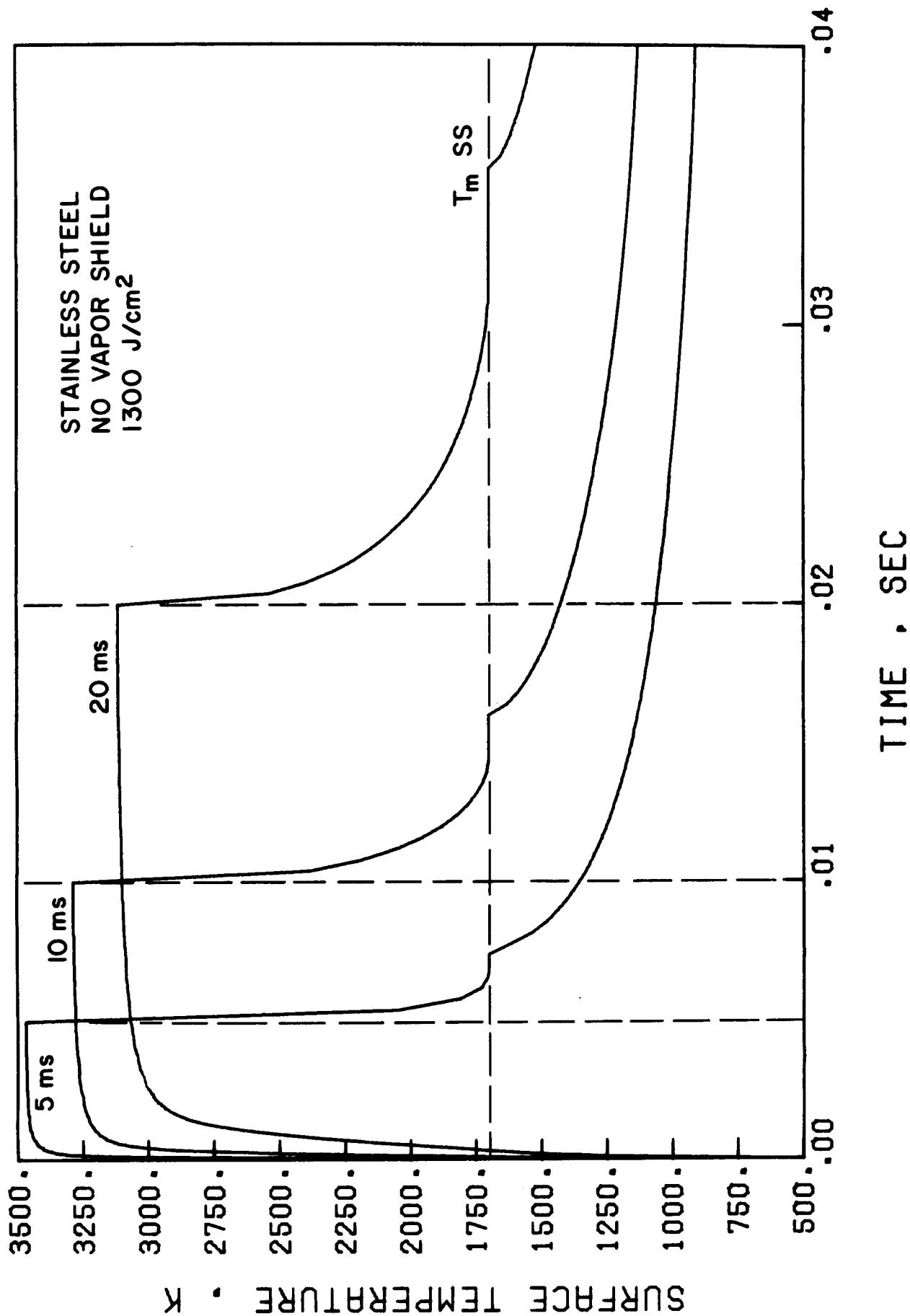


Figure 6 Surface temperature rise of stainless steel for energy density 1300 J/cm² and different disruption times (no vapor shielding).

disruption time the higher the surface temperature and the shorter the surface melt duration. Melt duration times are important when considering issues such as stability of the melt layer under different forces existing in the reactor chamber [11]. The resolidification time, which is defined as the total time liquid is present, is proportional to the disruption time, and is longer for longer disruption times. At the end of the disruption time, the surface temperature drops sharply and the material cools down. In Fig. 5, where the deposited energy is twice the value used in Fig. 4, the surface temperature is naturally higher and the rise in temperature is steeper. It can also be seen from Fig. 5 that the surface melt duration is somewhat shorter than the one shown in Fig. 4 for the cases of 5 and 10 ms disruption, but it is longer for the 20 ms case. The reason for this behavior will be explained later. Figure 6 shows the surface temperature for input energy density of 1300 J/cm^2 . Again the surface temperature is higher and remains high for longer duration. The temperature rise is steeper than for the other two cases of lower input energy. This in turn causes the evaporation to increase as will be shown later.

Comparing Figs. 4, 5, and 6 for the 20 ms disruption time, it can be seen that the surface melt duration is the longest for input energy densities around 650 J/cm^2 . The explanation for this behavior is that at high energy densities (1300 J/cm^2) a considerable amount of energy will be expended in vaporization, leaving a proportionately lower amount of energy for melting. At the lower energy densities (325 J/cm^2) there is simply not as much energy available to cause melting.

7.2 Comparison of Surface Temperatures

In this section we present a graphic comparison between the three different materials for the same case of 650 J/cm^2 and 10 ms disruption time.

Figure 7 shows the surface temperature rise for the three materials at these conditions. Although SS has the lowest surface temperature, its maximum surface temperature is much higher in relation to its melting point. Therefore, a stainless steel surface melts for a duration of about 20 ms under these disruption conditions. Carbon has a higher surface temperature than SS mainly because its initial temperature is taken as $T_0 = 1500^\circ\text{K}$ compared to $T_0 = 573^\circ\text{K}$ for both Mo and SS. Mo attains the maximum surface temperature, but the temperature rise is much slower than that for both carbon and stainless steel. For the disruption conditions considered, a Mo surface melts for a duration of about 10 ms.

7.3 Surface Velocity

The surface velocity, which is the velocity at which the front surface recedes as a result of evaporation, depends on the surface temperature as well as on material properties, such as vapor pressure. The integration of this velocity over the time gives the total amount of material evaporated.

A general feature of the surface velocity is that the shorter the disruption time the higher is the surface velocity and consequently, as will be shown later, the greater is the amount of material evaporated. Higher input energies not only increase significantly the surface velocity, but they also cause the surface to recede earlier in time. As a result, the vaporization is increased dramatically.

A comparison of the surface velocity for the three materials is shown in Fig. 8 for input energy density of 650 J/cm^2 and for 10 ms disruption time. Stainless steel has a higher surface velocity than carbon although carbon has the higher surface temperature. This can be explained by the lower vapor pressure of carbon relative to that for stainless steel. Molybdenum, for the

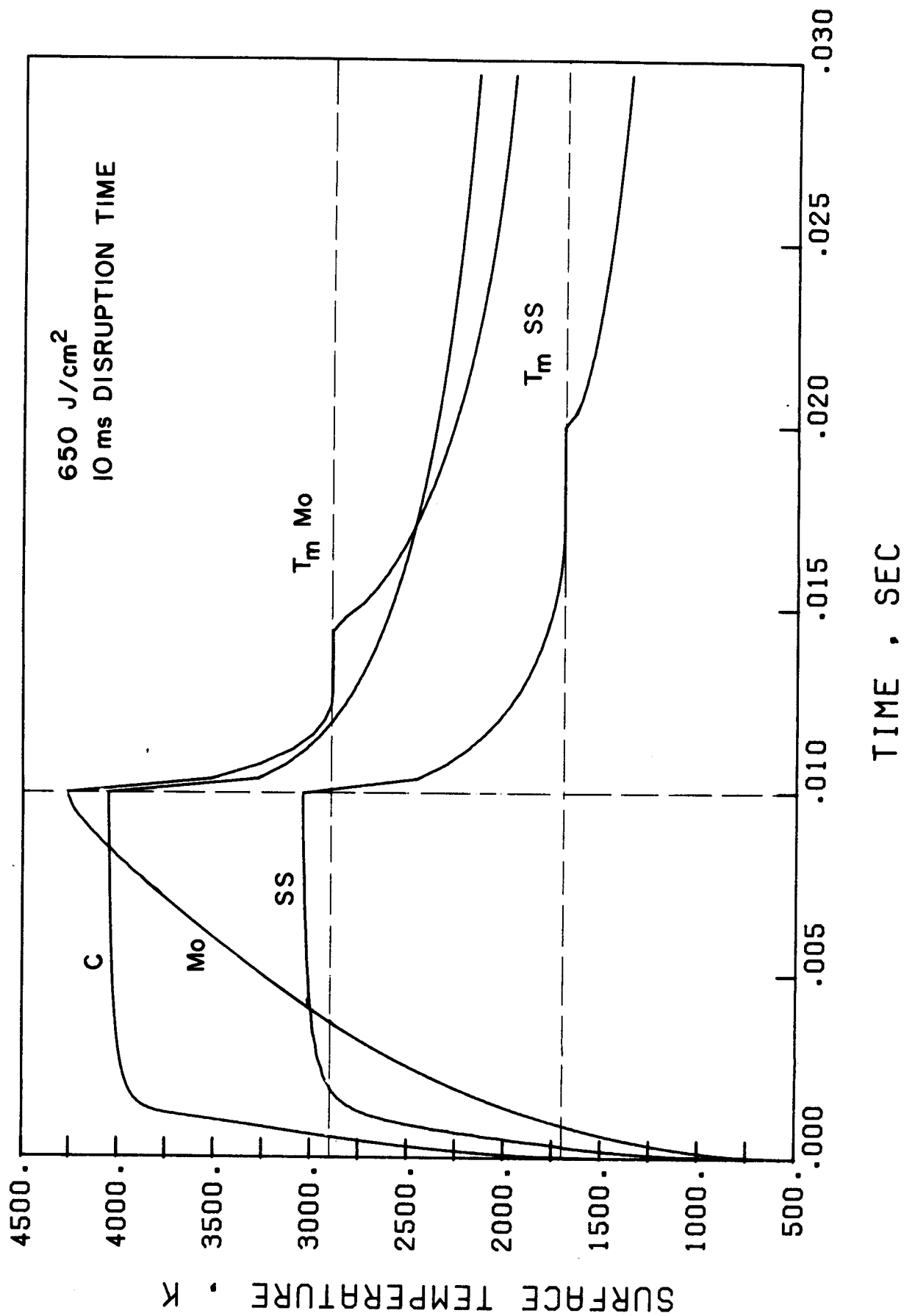


Figure 7 Comparison of surface temperature rise for SS, Mo, and C for energy density of 650 J/cm² and 10 ms disruption time (no vapor shield).

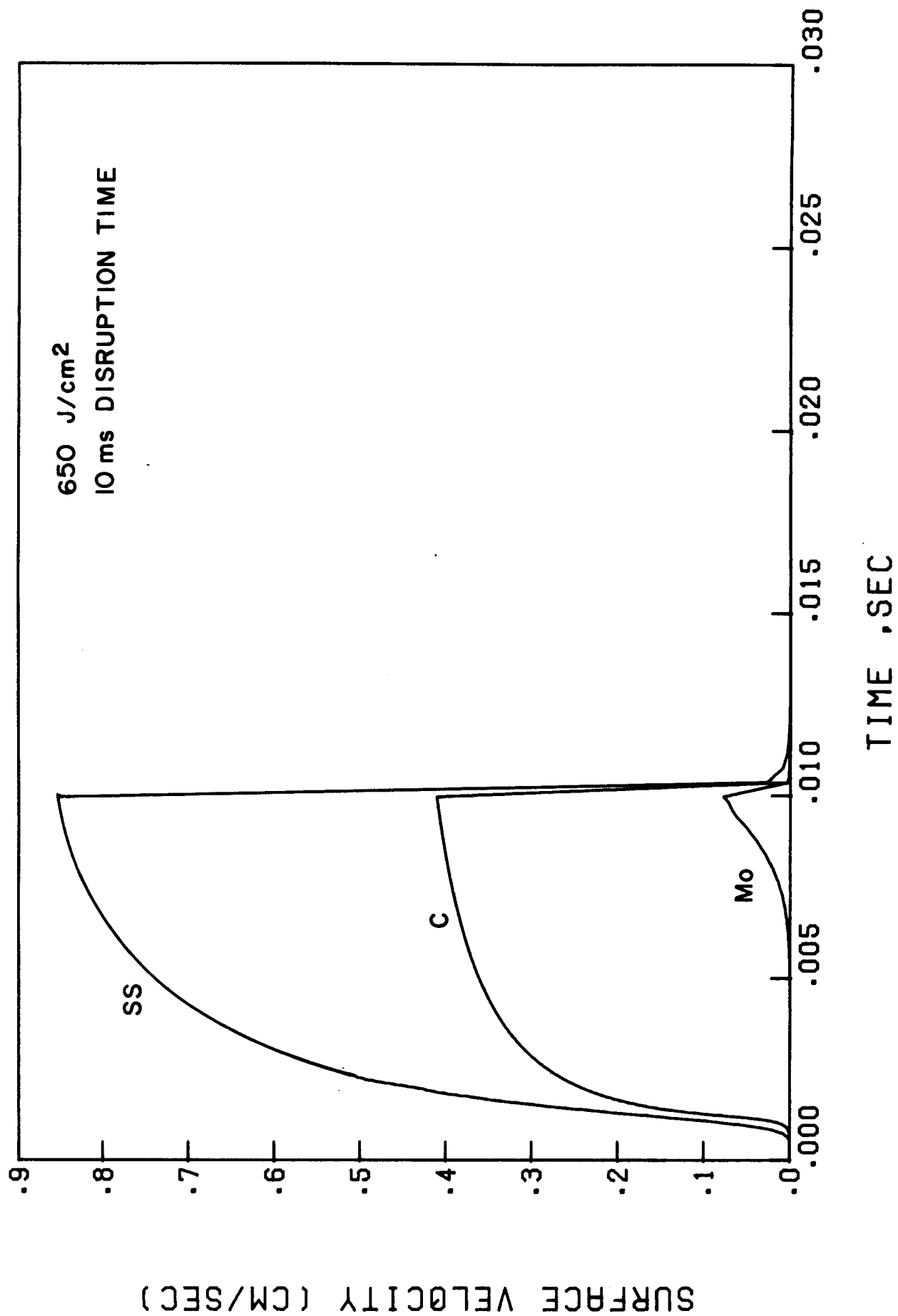


Figure 8 Surface velocity of SS, Mo and C for energy density of 650 J/cm² and 10 ms disruption time (no vapor shield).

same conditions, shows a very small surface velocity compared to stainless steel and carbon. Therefore, there is little evaporation of Mo for 650 J/cm^2 deposited in 10 ms.

7.4 Vapor Shielding

7.4.1 Effect of Vapor Shielding on Surface Temperature

The surface temperature of stainless steel as a function of time and for an energy density of 325 J/cm^2 is shown in Fig. 9 with vapor shielding included. The surface temperature has two peaks. The first peak is an indication that enough material has vaporized to effectively start shielding the wall. The subsequent temperature rise after the first peak is caused by the fact that the vapor reradiates some of its energy back to the wall. The second peak, i.e. the normal peak, occurs at the end of the disruption time, i.e. when the energy flux is terminated. The first peak, which is related to the vapor shielding, is short in duration and is shifted to shorter times with decreasing disruption time. Comparing Fig. 9 with Fig. 4, i.e. an identical case with and without vapor shielding, it can be seen that in case of vapor shielding the surface temperature is lower and the surface melt duration is shorter for input energy of 325 J/cm^2 . This means that less material is evaporated and thinner melt layers are developed. For large input energies of 1300 J/cm^2 , the case shown in Fig. 10, the surface temperature is lower and the rise in the temperature after the first peak is slower with vapor shielding as compared to the case in Fig. 6 without vapor shielding. The first peak occurs much earlier in time and is much shorter in duration than for the lower energy case. However, in contrast to the 325 J/cm^2 case, the melt duration is longer with the vapor shielding.

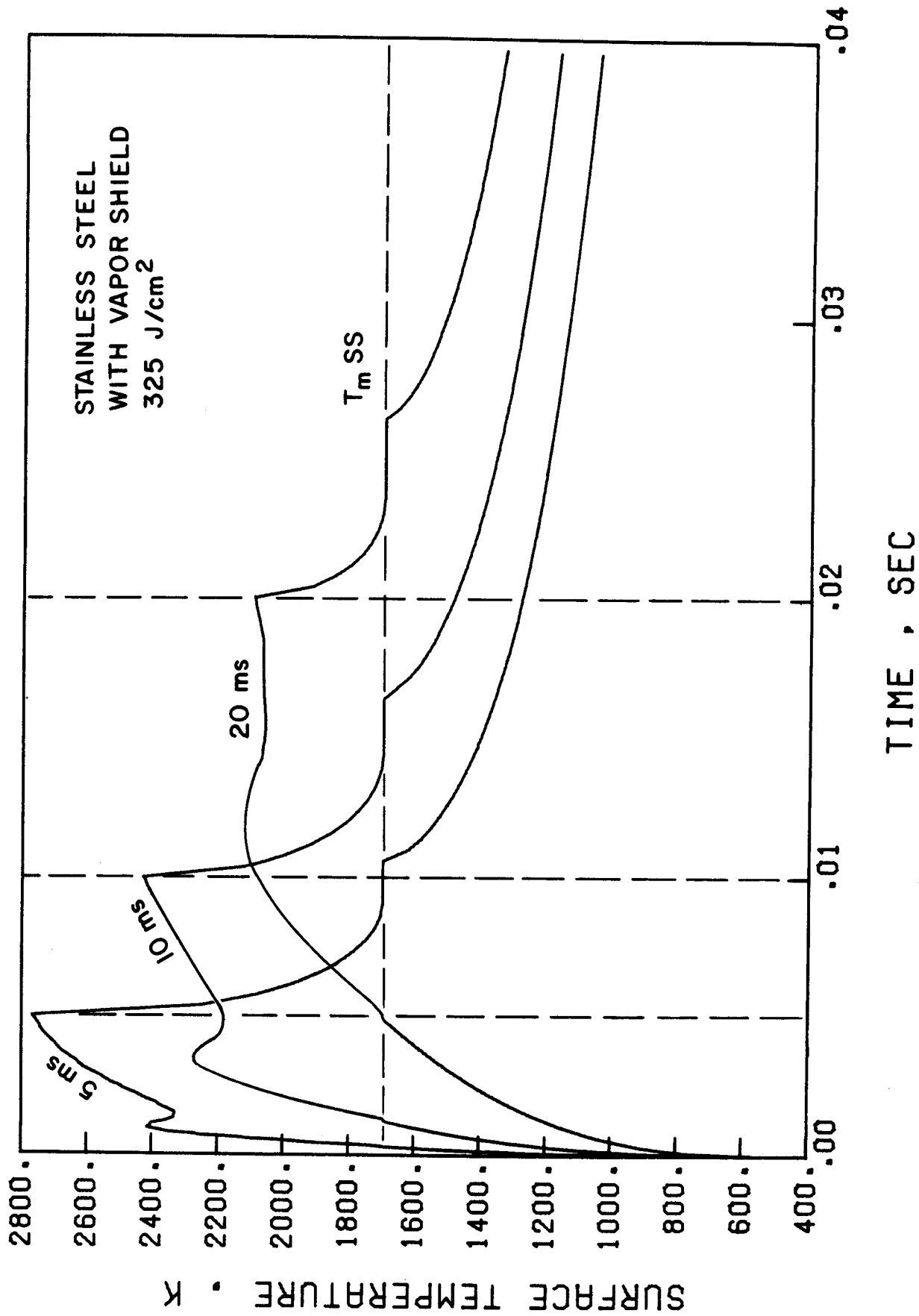


Figure 9 Surface temperature rise of stainless steel for energy density of 325 J/cm² and different disruption times with vapor shield.

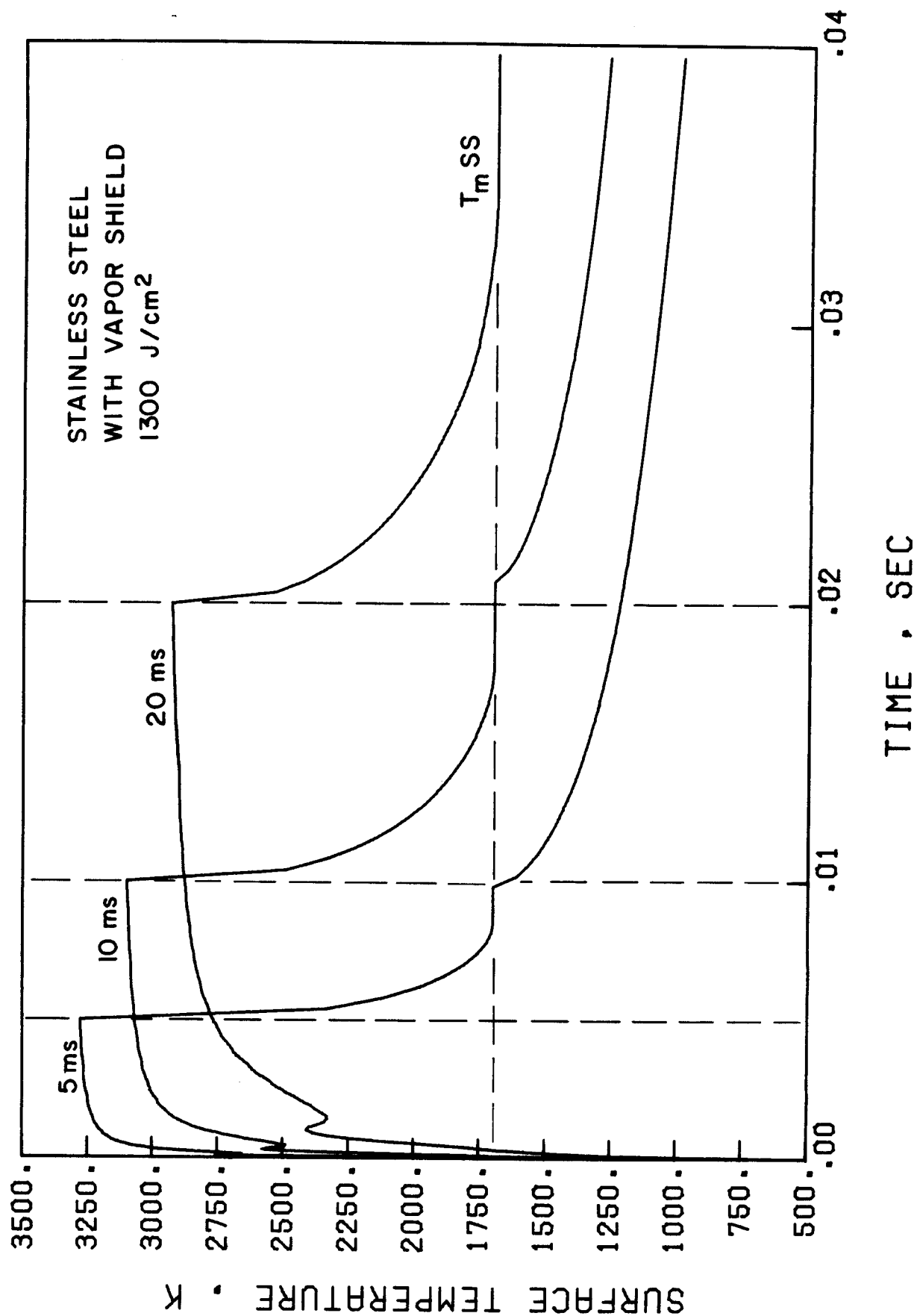


Figure 10 Surface temperature rise of stainless steel for energy density of 1300 J/cm² and different disruption times with vapor shield.

The effect of vapor shielding on the surface temperature is shown in Fig. 11 for the case where 650 J/cm^2 is deposited in 10 ms disruption time. The vapor shielding effectively decreases the surface temperature for C and SS compared to the case without shielding shown in Fig. 7. For Mo this suppression of the surface temperature rise due to vapor shielding is even more pronounced, so that the melt duration is now decreased. In contrast, the suppression of the surface temperature rise by vapor shielding in the case of SS prolongs the melt duration.

7.4.2 Effect of Vapor Shielding on Melt Thickness

The maximum melt thickness has been calculated for different disruption times and as a function of energy densities for stainless steel. The results are shown in Fig. 12. It can be seen from this figure that the maximum melt thickness (for energy densities greater than 300 J/cm^2) is larger for longer disruption times (20 ms). This can be explained readily by the fact that depositing the same energy in shorter times will suppress heat conduction, and consequently, the surface temperature will be higher. Higher surface temperatures lead to higher evaporation rates, consuming a larger fraction of the deposited energy and leaving less energy available for melting. It can also be seen from Fig. 12 that melting requires a minimum or threshold energy density flux. This threshold depends both on the material and the rate of energy deposition. With increasing energy density, the melt layer thickness rises rapidly, reaches a maximum, and then declines somewhat.

The maximum melt thickness for stainless steel with the vapor shielding effect is also shown in Fig. 12. No large differences arise in the general behavior when vapor shielding is included. At energy densities just above the threshold values, the vapor shielding tends to decrease the melt thickness,

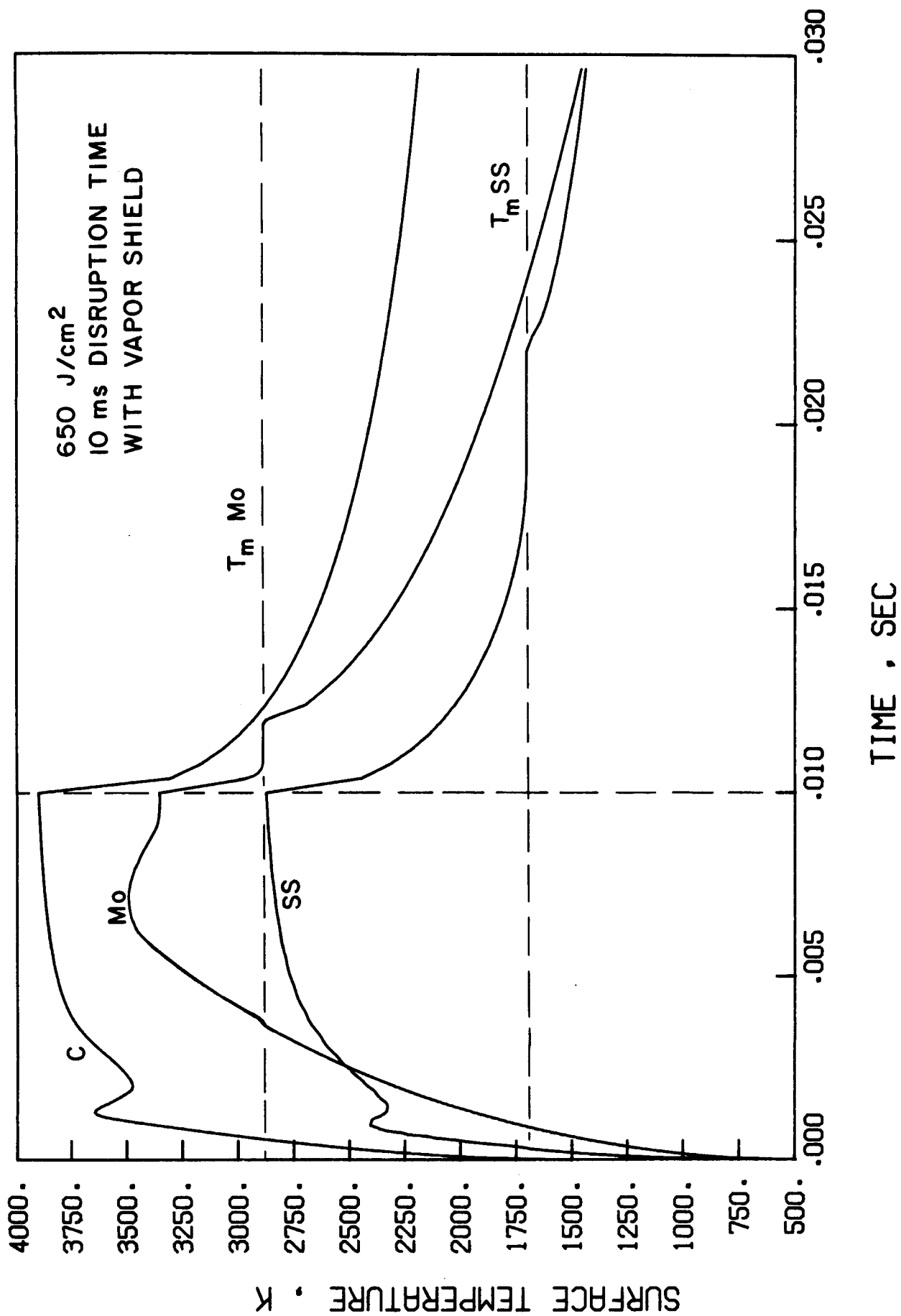


Figure 11 Surface temperature rise of SS, Mo and C for energy density of 650 J/cm² and 10 ms disruption time with vapor shield.

MELTING ZONE THICKNESS IN STEEL FOR DIFFERENT DISRUPTION TIMES

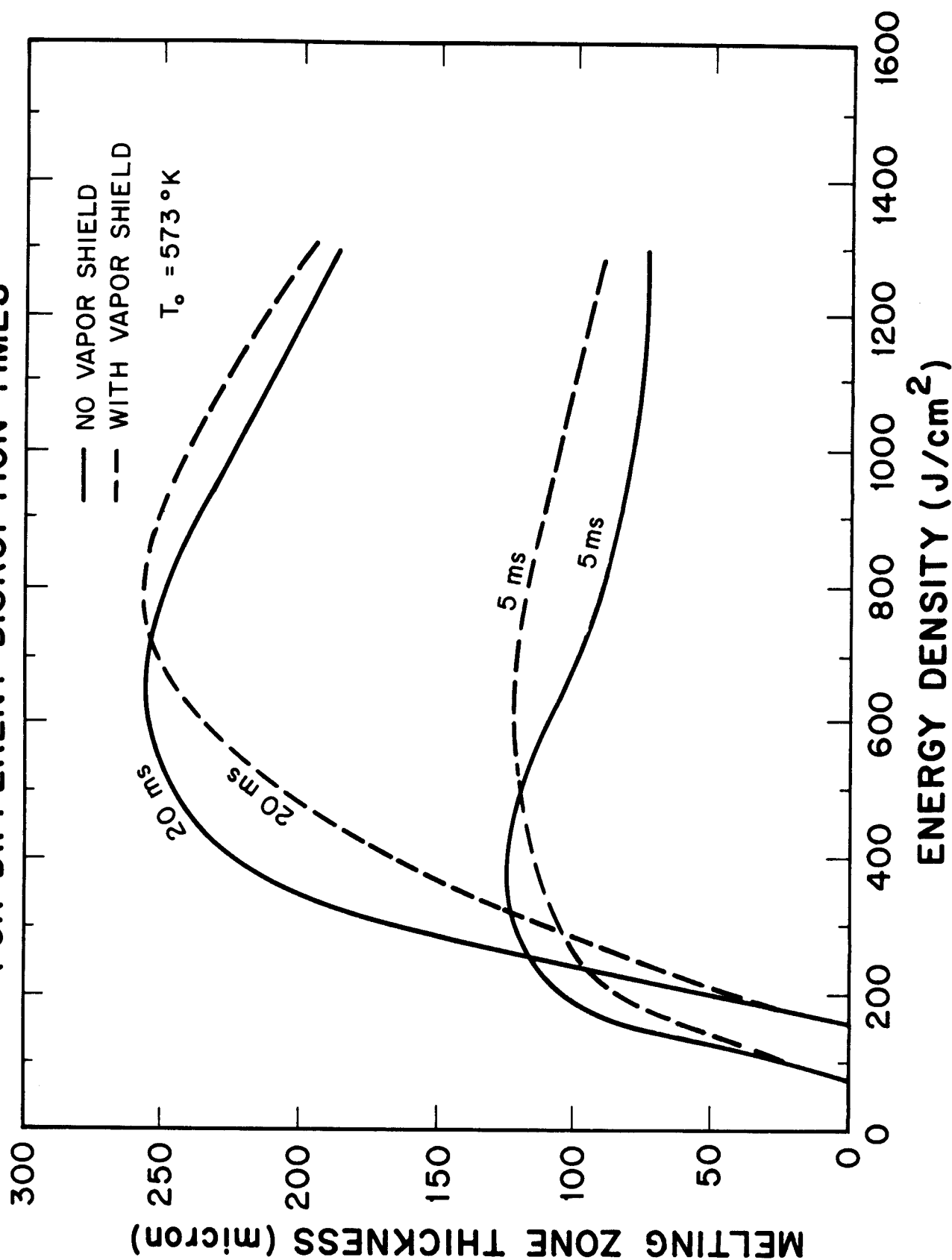


Figure 12 Effect of vapor shielding on melt layer thickness of stainless steel.

but at high energy densities the vapor shielding increases the melt thickness. This can be explained by the fact that at lower energy densities where there is just enough vapor developed to stop the incoming plasma ions, the heat flux from the vapor radiation is not sufficient to cause as much melting. On the other hand, at higher total energy densities the heat flux from the radiating vapor is not high enough to cause more evaporation; instead, most of the energy will now cause more melting.

The effect of vapor shielding on the Mo melt layer thickness is found to be larger than the effect on SS [28]. This is because the high melting point of Mo requires higher input energies to cause melting. When vapor shielding occurs, the input energy to the first wall decreases and melting decreases.

7.4.3 Effect of Vapor Shielding on the Material Vaporized

The total material evaporated is calculated by integrating the velocity of the receding surface over the time. Figure 13 shows the thickness of the evaporated layer for stainless steel for 1000 disruptions without and with vapor shielding. Whereas vapor shielding has only a minor effect on the melt layer thickness, it affects the evaporation by at least an order of magnitude. The insensitivity of the melt layer thickness to vapor shielding is due to the fact that melting of stainless steel precedes evaporation by a relatively large time interval. This is expected for all metals with a relatively low melting point. It can also be seen from Fig. 13 that the shorter the disruption time, the more material is evaporated. This is because at shorter disruption times, the surface temperature becomes higher as there is not enough time available for the heat to be conducted away. Higher temperatures mean higher receding velocities which in turn cause more material to evaporate.

MATERIAL EVAPORATED FOR DIFFERENT DISRUPTION TIMES

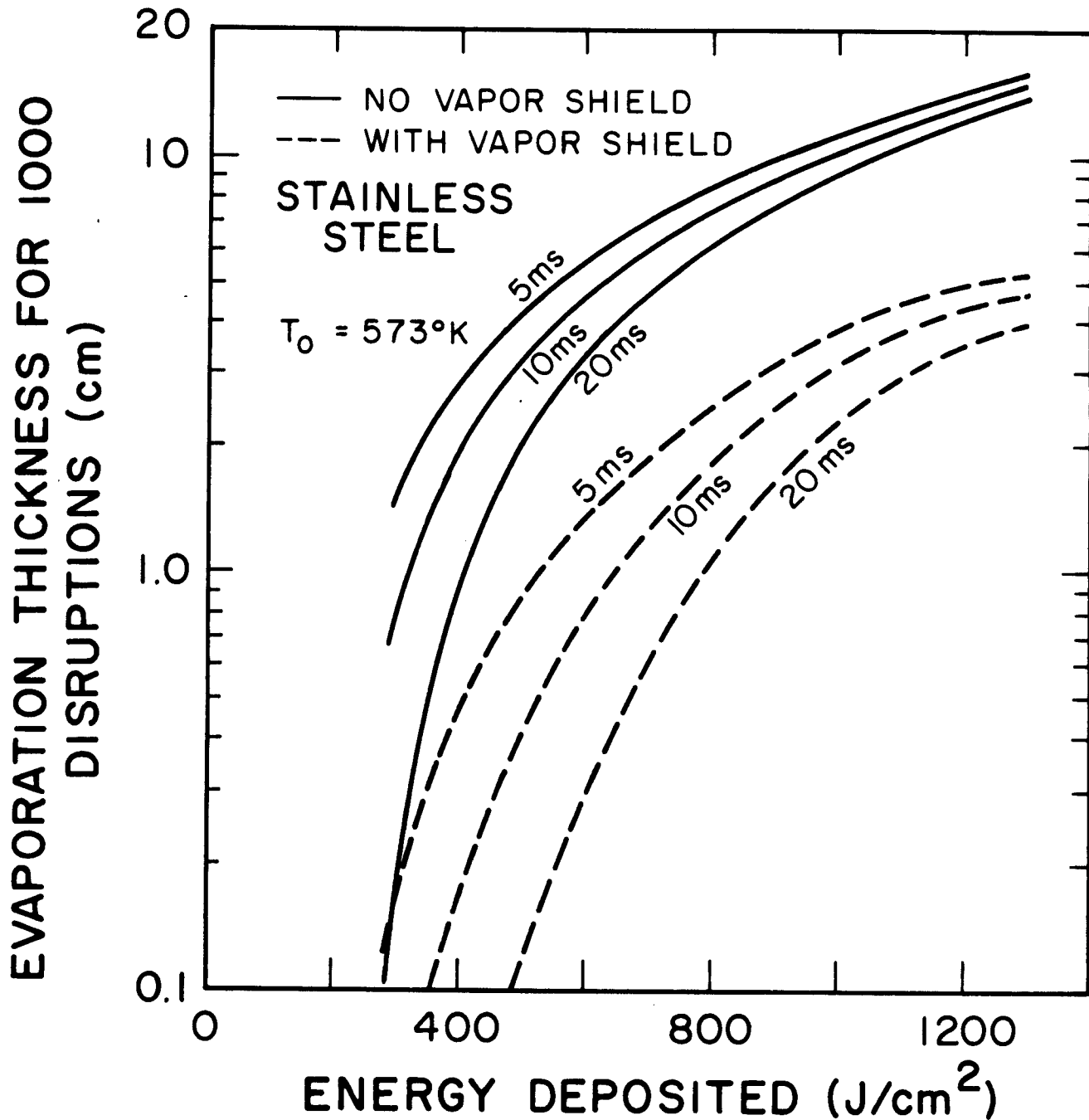


Figure 13 Evaporation thickness of stainless steel for 1000 disruptions for different energy deposited.

8. Effect of Disruption Time

There is great uncertainty as to the duration for plasma disruptions. For example, estimates range from 1 ms to possibly 100 ms, and in some cases, less than a millisecond. As seen from the previous results, the disruption time determines to a large degree whether melting, vaporization, or both will occur [28]. Figure 14 illustrates this point. It shows the thickness of both melted and evaporated material for stainless steel for an input energy density of 325 J/cm^2 ; disruption times range from 100 μs to 100 ms. At lower disruption times, most of the energy goes into vaporization. Then vaporization decreases as the disruption time becomes longer and for disruption times longer than 20 ms no significant vaporization occurs. Consequently, at lower disruption times no significant melting occurs simply because there is not enough time for the heat to be conducted into the bulk. As the disruption time becomes longer, the amount of melted material rises rapidly, reaching a maximum around 20 ms, and then decreases. For disruption times greater than 80 ms there is no melting at all. For higher input energy densities this general behavior for the melted and evaporated material as a function of the disruption time is preserved. However, the total amount of the evaporated and melted material increases, and the maximum melt thickness is found at larger disruption times [28]. It should be noted that if the melted material is sloughed off the surface as fast as it is formed, the total material removed from the surface will be much more than just the total sum of the melted and vaporized material shown in Fig. 14. In this case, most of the energy would be expended in melting and little in evaporation. As the heat of fusion is much less than the heat of evaporation, the total melt thickness would greatly exceed that obtained for a stationary melt layer.

EVAPORATED AND MELTED MATERIAL AS A FUNCTION OF DISRUPTION TIME

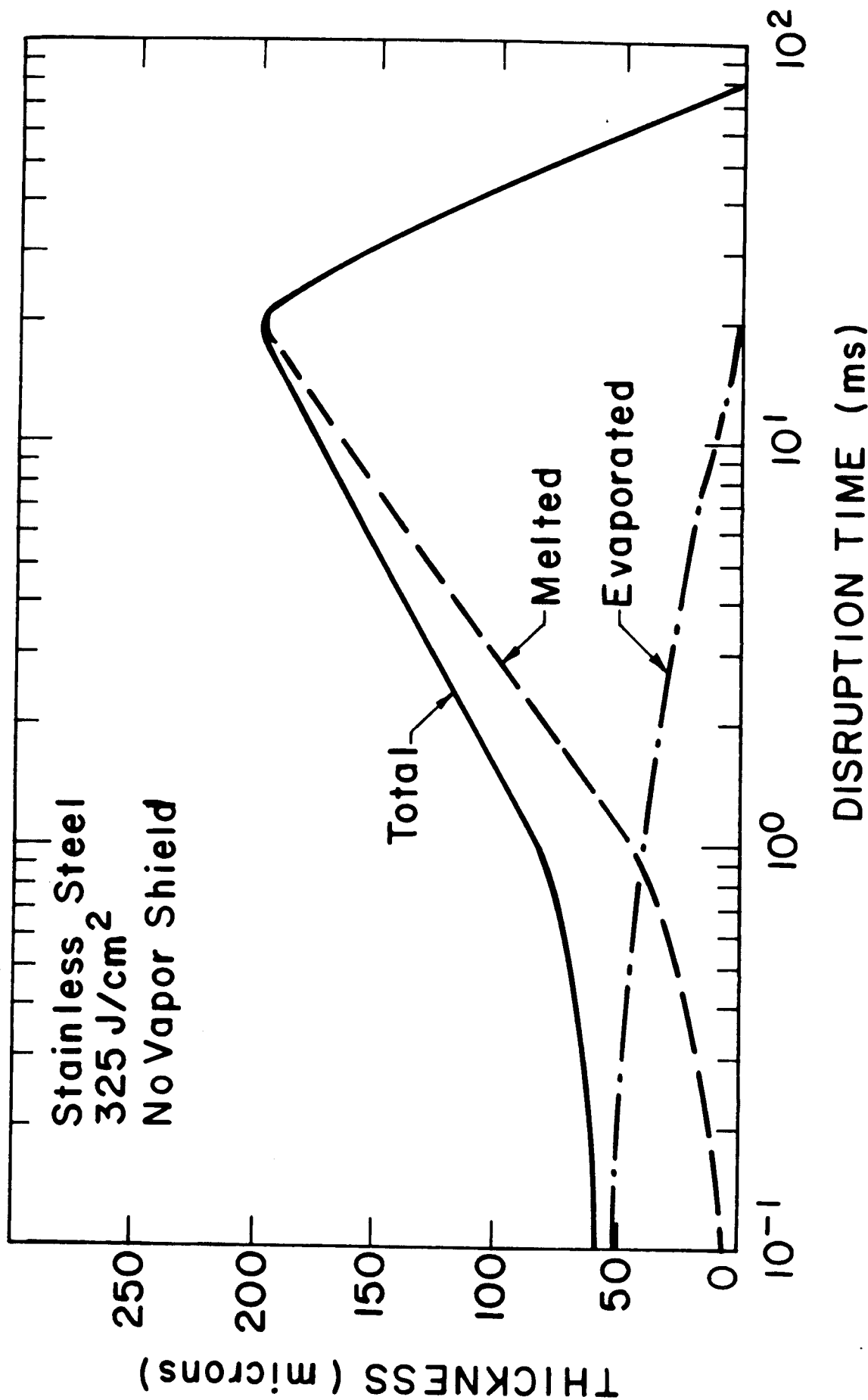


Figure 14 Effect of disruption on the amount of melted and evaporated material from SS for 325 J/cm² with no vapor shield.

9. Effect of Pulse Shape

The effect of different pulse shapes on the surface temperature and on the amount of material melted and evaporated has been studied by considering two different shapes, square and triangular pulses. Figure 15 shows the surface temperature as a function of time for an energy density of 325 J/cm^2 deposited in 10 ms. It can be seen that stainless steel has a higher surface temperature with the triangular pulse than for the square pulse. This will cause more material to evaporate for the triangular pulse. This can be seen from Fig. 16 where the surface velocity for both pulses is plotted as a function of time. The integration of this velocity over the time is found to result in 25% more evaporation for the triangular pulse. It can also be seen from Fig. 15 that stainless steel has a shorter surface melt duration for the triangular pulse than for the square pulse. This means that less material is melted with a triangular pulse. For the case given above, it is found that the triangular pulse would decrease the melt thickness by about 15% compared to the square pulse.

10. Conclusions

Models were developed to solve the heat conduction problem with phase changes and two moving boundaries, and they have been applied to study melting and evaporation during plasma disruptions. Results are shown for stainless steel, Mo, and graphite as first wall materials. The following conclusions can be drawn from this study:

1. Vapor shielding by the stopping of plasma ions in the evolving vapor leads in turn to a significant reduction of the material further evaporated.

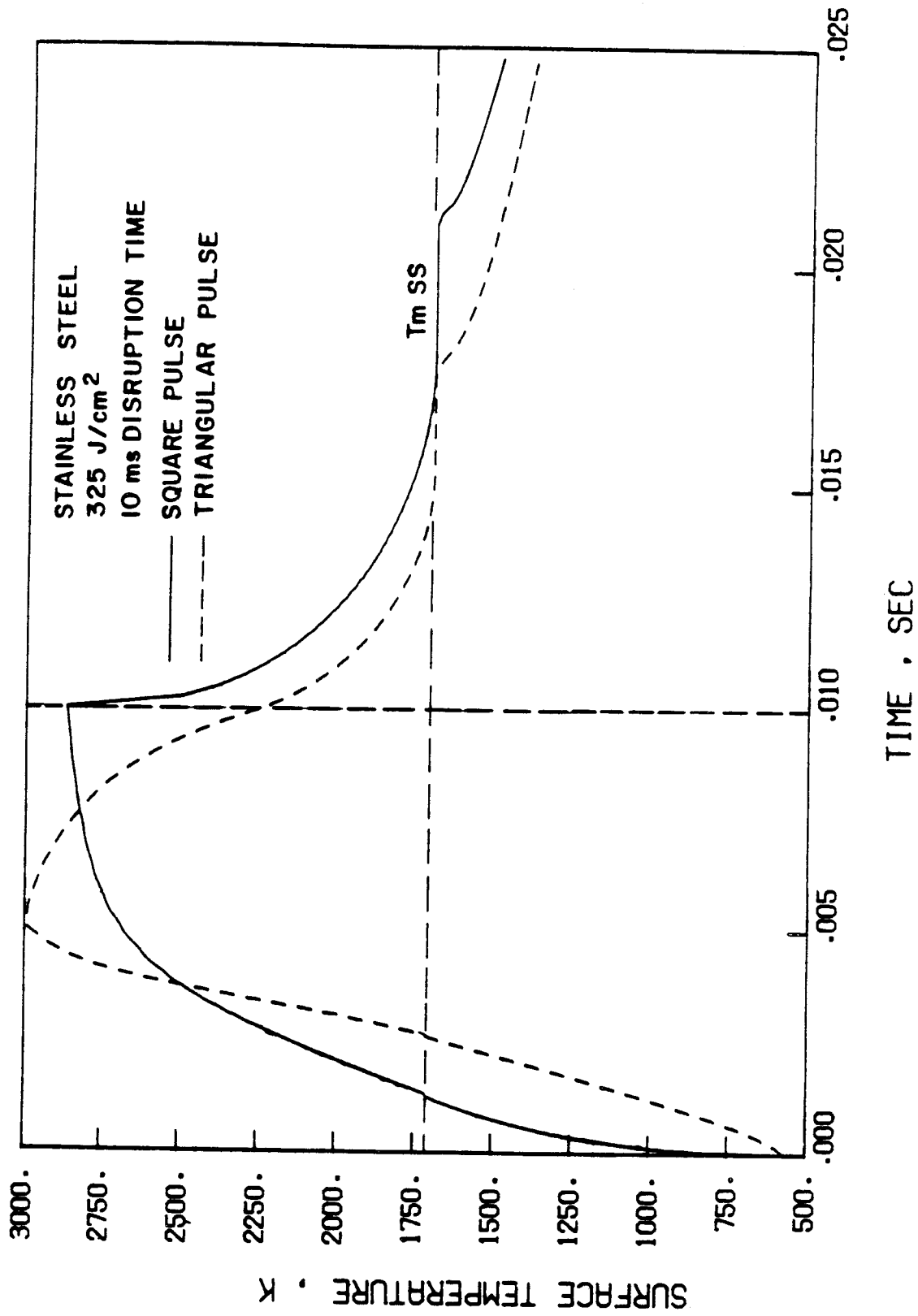


Figure 15 Comparison of SS surface temperature rise for square and triangular pulse shape.

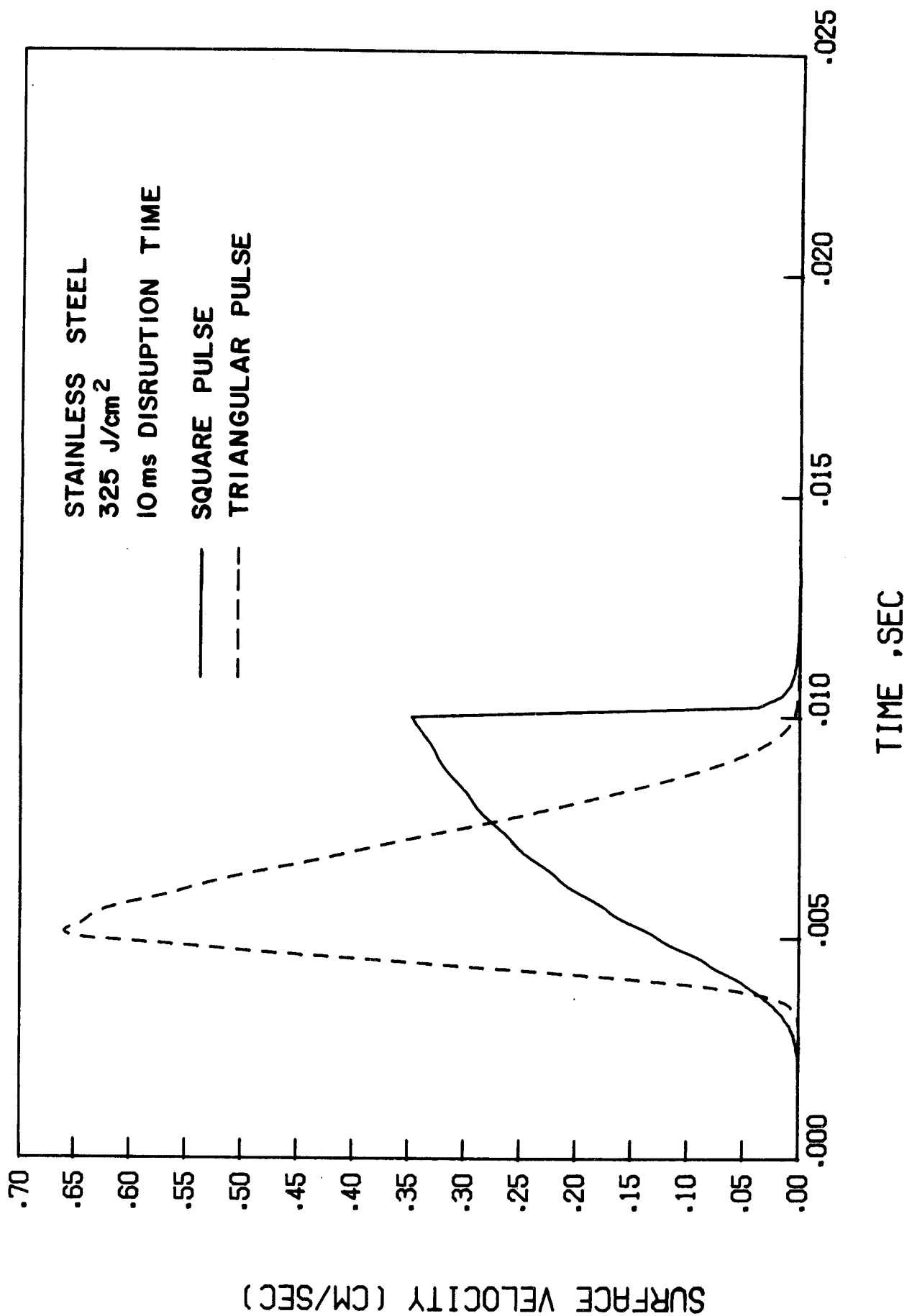


Figure 16 Comparison of SS surface velocity for square and triangular input pulses.

2. At lower energies, near the threshold, vapor shielding tends to decrease both melting and evaporated material. But at higher energies than this threshold, vapor shielding decreases the evaporation and slightly increases the melt thickness.
3. Evaporation from Mo is substantially less than for both stainless steel and carbon for the same input energy densities and disruption times.
4. Different disruption pulse shapes can substantially change the thickness of melted and vaporized material.

Acknowledgment

Support for this work has been provided by the U.S. Department of Energy, Japan Atomic Energy Research Institute (JAERI), and the Wisconsin Electric Utilities Research Foundation (WEURF).

References

- [1] G.G. Dolgov-Savelier et al., Sov. Phys.-JETP 11 (1960) 287.
- [2] S.A. Cohen et al., Nuclear Fusion 21 (1981) 233.
- [3] M.M. Sabado et al., General Atomic Report GA-A15633, October 1979.
- [4] R. Behrisch, Nuclear Fusion 12 (1972) 695.
- [5] R. Behrisch, J. Nucl. Mater. 85 & 86 (1979) 1047.
- [6] L.L. Loebel and W.G. Wolfer, University of Wisconsin Report UWFD-370 (1980).
- [7] INTOR, Zero Phase, Intern. Atomic Energy Agency, Vienna (1980).
- [8] The fusion engineering device, Dept. of Energy Report, DOE/TK-11600 (October 1981).
- [9] STARFIRE - a commercial tokamak fusion power plant study, Argonne National Laboratory Report, ANL/FPP-80-1 (September 1980).
- [10] J. Rawls, Private Communication.
- [11] W.G. Wolfer and A.M. Hassanein, J. Nucl. Mater. (to be published).
- [12] M.N. Özisik, Heat conduction, Wiley-Interscience, New York (1980).
- [13] J.C. Muehlbauer and J.E. Sunderland, Applied Mechanics Reviews 18 (1965) 951.
- [14] J.R. Okkendon, and W.R. Hodgkins, Editors, Moving boundary problems in heat flow and diffusion, Clarendon Press, Oxford 1975.
- [15] D. Wilson, A. Solomon, P. Boggs, Editors, Moving boundary problems, Academic Press, New York 1978.
- [16] J.F. Ready, Appl. Phys. Letters 3 (1963) 11.
- [17] J.F. Ready, J. Appl. Phys. 36 (1965) 2.
- [18] J.G. Andrews and D.R. Atthey, J. Inst. Maths. Appl. 15 (1975) 59.

- [19] B.A. Osadin and G.I. Shapovalov, *Teplofizika Vysokikh Temp.* 10 (1972) 361.
- [20] N.N. Golodenko and V.M. Kuz'michev, *Teplofizika Vysokikh Temp.* 10 (1972) 1126.
- [21] J. Crank and P. Nicholson, *Proc. Camb. Phil. Soc.* 43 (1947) 50.
- [22] D.W. Peaceman and H.H. Rachford, *J. Soc. Indust. Appl. Math.* 3 (1955) 28.
- [23] J.P. Hirth and G.M. Pound, *Prog. Mater. Sciences* 11 (1963), Pergamon Press.
- [24] Ya.B. Zel'dovich and Yu.P. Raizer, *Physics of Shock Waves and High Temperature Hydrodynamic Phenomena*, Vol. 1, Academic Press, New York (1966).
- [25] R.W. Schrage, *A theoretical study of interphase mass transfer*, Columbia Univ. Press, New York (1953).
- [26] S.I. Anisimov and A.Kh. Rakhmatulina, *Sov. Phys. JETP* 37 (1973) 441.
- [27] J.D. Callen, Private Communication.
- [28] A.M. Hassanein, Thesis, University of Wisconsin Report UWFDM-465 (1982).
- [29] S. Kim Choong, *Thermophysical properties of stainless steels*, Argonne National Laboratory Report ANL-75-55 (1975).
- [30] G. Betz and M.G. Frohbert,, *High Temp.-High Pressures* 12 (1980) 169.
- [31] V. Seydel, H. Bauhof, W. Fucke, H. Wadle, *High Temp.-High Pressures* 11 (1979) 635.
- [32] N.S. Rasor and J.D. McClelland, *J. Phys. Chem. Solids* 15 (1959) 17.